scientific reports

Check for updates

OPEN

Electrical manipulation of the spins in phosphorene double quantum dots

Tanmay Thakur[1,2], Francois M. Peeters[2,3,4] & Bartłomiej Szafran[1]✉

We investigate electric dipole spin resonance (EDSR) induced by an oscillating electric field within a system of double quantum dots formed electrostatically in monolayer phosphorene. Apart from the observed anisotropy of effective masses, phosphorene has been predicted to exhibit anisotropic spin-orbit coupling. Here, we examine a system consisting of two electrons confined in double quantum dots. A single-band effective Hamiltonian together with the configuration interaction theory is implemented to simulate the time evolution of the ground state. We examine spin flips resulting from singlet-triplet transitions driven by external AC electric fields, both near and away from the Pauli blockade regime, revealing fast sub-nanosecond transition times. Furthermore, we analyze the impact of anisotropy by comparing dots arranged along a different crystal axis. The sub-harmonic multi-photon transitions and Landau-Zener-Stückelberg-Majorana transitions are discussed. We show modulation of spin-like and charge-like characteristics of the qubit through potential detuning.

In the fast-evolving landscape of quantum technology, precise control and manipulation of spin emerges as a topic of prime importance. Coupling of spin with the magnetic field facilitates the control of electron spins in the system. If this magnetic field has an alternating component, it induces rotation of spin on the Bloch sphere by electron spin resonance (ESR)[1–3] and thus one of the simplest spin manipulation can be achieved. Such spin rotations are crucial in spintronics[4–6] and quantum computing applications[6–8]. However, because of the small moments of the spin, a very strong alternating magnetic field is required to realise fast rotations, making ESR a demanding experimental task. Spin-orbit coupling (SOC) in the materials, either inherent or engineered[9,10], offers a practical alternative for this task by coupling the spin moment to the electric field through electric dipole spin resonance (EDSR)[11,12]. It is an optimal choice for spin manipulations, since a fine-tuned electric field of desired features can be produced using advanced engineering methods. Although EDSR is observed in a variety of systems like bulk crystals[11,13] and quantum wells[14,15], its ideal use is in quantum dots where discrete states can be used as a qubit[16–18].

The EDSR is investigated in double quantum dots with two electrons, with spin manipulations lifting the Pauli spin blockade of the current flow[19,20]. SOC hybridization between the spin singlet and triplet states results in an avoided crossing, which can be used to determine the SOC energy[21]. Effects of tunneling with the SOC in strongly electrically driven double quantum dot system were examined theoretically[22,23] and showed a nonlinear character of the spin resonance. Spins in III-V semiconductor quantum dots are subject to dephasing due to electron-nucleus effects[24–26] which, when comparable with the spin-flip times, will hinder precise spin control. For this reason, fast manipulation and control of the spins are pursued by researchers[10,26] and remains a considerable challenge to develop quantum dots as qubits. The states of the bottom of the conduction band in phosphorene are constructed of p-type orbitals[27] which eliminates the dephasing effects of the hyperfine interaction.

The anisotropic spin-orbit magnetic field, produced by combined Rashba and Dresselhaus SOC, results in anisotropic avoided crossings and relaxation times[28–30]. Such anisotropy affects also the rate of spin-flip tunneling in double quantum dots. A similar but inherent anisotropy in Rashba SOC alone was predicted in phosphorene[31,32]. The phoshophorene has an inversion symmetry and the Dresselhaus coupling occurs only when the symmetry is intentionally broken[33].

Phosphorene[34], a monolayer form of black phosphorous, is a material with rapidly evolving interest and is extensively studied for its strongly correlated properties[35–37] and anisotropic characteristics[38,39]. The band's anisotropy reflects itself in the effective masses of the electron in phosphorene and results in different Rashba SOC

[1]Faculty of Physics and Applied Computer Science, AGH University of Krakow, al. Mickiewicza 30, 30-059 Kraków, Poland. [2]Department of Physics, University of Antwerp, Groenenborgerlaan 171, 2020 Antwerp, Belgium. [3]Nanjing University of Information Science and Technology, Nanjing 210044, China. [4]Departamento de Física, Universidade Federal do Ceará, Campus do Pici, Fortaleza, Ceará 60455-900, Brazil. ✉email: bszafran@agh.edu.pl

parameters for zig-zag and armchair direction. Phosphorene quantum dots in the form of nano flakes have been studied for various applications[40,41]. In this work, we study electrostatically confined double quantum dots in phosphorene with electric field driving. This system is promising to study the majority of the physics concerned with quantum spin control. We investigate the interplay between the anisotropy of the effective masses, tunneling and SOC and spin flip-rates. We also examine the effects of asymmetry of the dot potentials, which can be exploited as a control knob in experiments to fine-tune the nature of qubit and spin manipulations. Additionally, we take a look at low frequency electric driving, i.e. Landau-Zener[42,43] sweep near the avoided crossing of the lowest energy spin-singlet and spin-triplet states of double quantum dot. We will also see the occurrence of spin-flip transitions, which are forbidden by parity selection rules through higher order processes and explain the mechanism behind it.

The paper is organised as follows: In Sect. "Theory", we discuss the theory and setup that were considered to study the system. Then we move on to the discussion of our results in Sect. "Results & discussions", where we first discuss the effects of asymmetry on the system in Sect. "Effects of asymmetry at t=0" and study the main focus of the work of spin manipulations and spin-flip transitions in Sect. Spin-flip transitions. Later in Sect. Dots arranged in the zig-zag direction we discuss the effects of anisotropy of phosphorene by changing the arrangement of the dots in a different lattice direction. Finally, we conclude and summarize our results in Sect. Summary and conclusions.

Theory

The system under consideration is lateral double quantum dots with spin orbit coupling, external constant perpendicular magnetic field and external time dependent electric field as illustrated in Fig. 1. The single electron the Hamiltonian is,

$$H(t) = H_0 + H_{SO} + V'(t), \tag{1}$$

where H_0 is the effective mass continuum model for phosphorene derived from the tight-binding Hamiltonian[44], H_{SO} is the spin-orbit coupling and $V'(t)$ is the external time dependent electric field for the control of spins in the dots. The single electron effective mass Hamiltonian is given by

$$\begin{aligned} H_0 =& \left(-i\hbar\frac{\partial}{\partial x} + eA_x\right)^2 / 2m_x + \left(-i\hbar\frac{\partial}{\partial y} + eA_y\right)^2 / 2m_y \\ &+ g\,\mu_B B\,\sigma_z\,/\,2 + V(x,y), \end{aligned} \tag{2}$$

with effective masses $m_x = 0.17037m_0$ ($m_y = 0.85327m_0$) along armchair (zig-zag) direction of the phosphorene crystal. The Landé g-factor for the material is taken to be $g = 2$. The corrections to the bare g-factor for phosphorene vary and are reported in previous theoretical[45,46] and experimental works[47,48]. The precise value of the g-factor is of less significance for our work as variations primarily impact the position of avoided crossings rather than qualitative conclusions regarding the spin control and spin-flip transitions.

The confinement potential $V(x, y)$ is modelled by two inverted Gaussians centered at $+d$ and $-d$ (c.f.Fig. 1) in the x (armchair) direction with parameters $d = 8$ nm, $s = 7$ nm and is given by

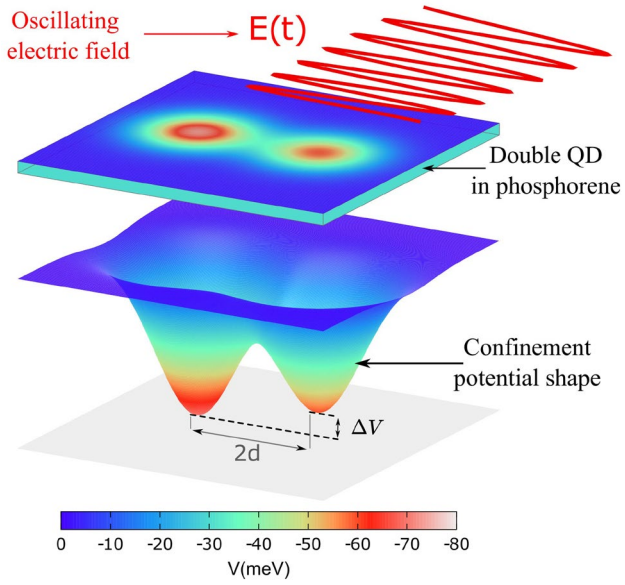

Figure 1. Schematic of the system under consideration showing double quantum dot formed in phosphorene due to electrostatic confinement potential and the applied oscillating electric field for driving the transitions.

$$V(x,y) = V_R \exp\left(-\frac{((x-d)^2+y^2)}{s^2}\right) + V_L \exp\left(-\frac{((x+d)^2+y^2)}{s^2}\right). \tag{3}$$

For the case of phosphorene electrons with strong correlation effects[49–51], as well as transitions induced by external driving fields, it is anticipated that higher energy states will have contributions to the physics of the system. While the parabolic potential serves as a convenient approximation for examining quantum dots near the ground states, we expect that the Gaussian potential will be a more realistic model for EDSR experiments involving quantum dots in phosphorene[52].

The spin-orbit coupling is a relativistic effect where the electric field induces a momentum dependent magnetic field which then couples with the spin. These effects especially in 2D materials were reviewed in Ref.[53]. This coupling is essential for driving the spins electrically and the contribution of this interaction is given by

$$H_{SO} = \lambda_x\left(-i\hbar\frac{\partial}{\partial x}\right)\sigma_y + \lambda_y\left(-i\hbar\frac{\partial}{\partial y}\right)\sigma_x, \tag{4}$$

where σ_x and σ_y are Pauli matrices and the anisotropic Rashba parameters are $\lambda_x = -17.9$ meV$\cdot$Å and $\lambda_y = 10.3$ meV$\cdot$Å. The values are taken to be ten times of that found by Farzaneh et. al for electric field of about 1 V/nm[31]. Another work[32] reported much larger anisotropy and values with external field of about 2.6 V/Å. In comparison, Shubnikov-de Haas oscillations and spin precession studies for InAs quantum well gives a Rashba parameter of 67.1 meV Å[54]. Experiments on other InAs heterostructures reported similar values[55–57]. Many other materials have been reported to have a larger SOC parameter than phosphorene[58] and phosphorene can be considered to have weak spin orbit coupling but which is order of magnitude larger than for graphene.

In order to induce transitions, driving electric field $E(t)$ can be applied experimentally with microwave radiation or simply by adding an AC voltage component to the confinement gate electrodes[25,59–67]. In both cases the wavelength of the electric field is much larger than that of the dimensions of the system. Therefore the in-plane electric field $V'(x,y,t)$ is taken to be spatially constant between the gates or throughout the size of the system. For field along x (armchair) direction,i.e. in the same orientation as the dots are arranged, the term $V'(t)$ in Eq. (1) equates to $V'(t) = -eFx\Theta(t)\sin(\omega t)$ and the field is switched on at $t = 0$, where $\Theta(t)$ is Heaviside function.

We focus on double quantum dots populated with two interacting electrons. Hence, the Hamiltonian of the complete system is given by,

$$H_{2e}(t) = \sum_{i=1}^{2} H_i(t) + \sum_{j>i}^{2} \frac{e^2}{4\pi\epsilon_0\epsilon\, r_{ij}}, \tag{5}$$

where the dielectric constant is $\epsilon = 9$. For the diagonalization of the final Hamiltonian in Eq. (5) at $t = 0$, we use the configuration interaction approach. The single electron eigenstates of the Hamiltonian $H_0 + H_{SO}$ are used to form Slater determinants for the possible configurations of two electrons in these eigenstates. The single electron eigenstates are themselves obtained using the discretization as performed in previous work[50]. The final Hamiltonian is then diagonalized in the basis of these Slater determinants to get the stationary states $|i\rangle$ and corresponding energies of $H_{2e}(t = 0)$. The states $|i\rangle$ is the total wavefunction containing spatial, spin and orbital state. The probability density of two electrons in state $|i\rangle$ is obtained using

$$\rho_i(\mathbf{r}) = \langle i| \sum_{i=1}^{2} \delta(\mathbf{r} - \mathbf{r}_i)\, |i\rangle. \tag{6}$$

Time dependent part of the Hamiltonian is solved subsequently using the Schrödinger equation. We assume that the final state of the system after the application of the time dependent field will be a linear combination of the original two electron energy eigenfunctions at $t = 0$. Moreover, we assume the time evolution of the individual states itself is given by the time dependent Schrödinger equation without the field $V'(t)$ and the extra potential evolves the coefficients of the linear combinations only. The final state is thus, $|\Psi(t)\rangle = \sum_i c_i(t)\ \exp[-iE_i t\hbar]\,|i\rangle$ and the probability of system to be in state $|n\rangle$ at time t is then $|c_n(t)|^2$. Substituting this state into the time-dependent Schrödinger equation one obtains the coupled differential equations for the time evolution of the coefficients,

$$i\hbar\left(\frac{d}{dt}\right) c_n(t) = -\,eF \sum_m c_m(t)\, exp[i(E_m - E_n)t/\hbar] \cdot \sin(\omega t)\, \langle m|x_1 + x_2|n\rangle. \tag{7}$$

The coupled differential equations are then solved using the Crank-Nicolson method to obtain the probabilities $|c_n(t)|^2$ at any given time. The system is evolved for a finite time with a fixed initial condition $c_i(t = 0) = \delta_{i1}$.

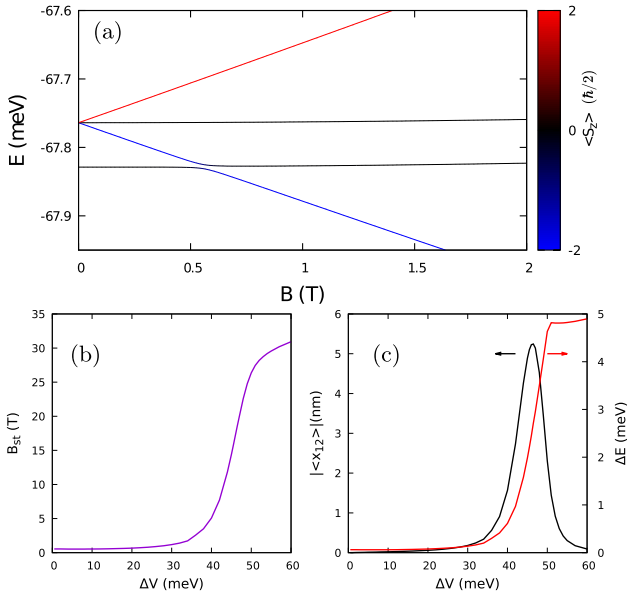

Figure 2. (**a**) Lowest energy eigenstates without the external electric field with the singlet-triplet avoided crossing at $B_{st} = 0.56$ T for $\Delta V = 0$. The color scale shows the average eigenvalue of S_z operator. (**b**) The magnetic field corresponding to the center of singlet-triplet avoided crossing as a function of asymmetry of the double dot system. (**c**) The maximal value of matrix element (black curve, left axis) at center if the avoided crossing and the singlet-triplet energy difference (red curve, right axis) as function of asymmetry.

Results & discussions

Effects of asymmetry at t=o

Figure 2a illustrates the two electron lowest eigenstates of the system at time $t = 0$. With a symmetric potential, where V_L and V_R are equivalent [as defined in Eq. (3)], the singlet state emerges as the ground state, accompanied by the triplet state as the first excited state with $\langle S_z \rangle = -\hbar$. External magnetic field along z-axis promotes the triplet as ground state, eventually. As a result, a crossing between the singlet and triplet states occurs which turns into an anti-crossing by the SO coupling. As we remove the symmetry by increasing $\Delta V = V_L - V_R$, the position of this avoided crossing shifts, as shown in Fig. 2b. The magnetic field at the center of this singlet-triplet (S/T) avoided crossing B_{ac} varies slowly for initial values of ΔV and increases rapidly after 40 meV and starts to saturate near 60 meV, suggesting that the system is sensitive to even small changes in potential between $\Delta V = 40$ meV and $\Delta V = 50$ meV. The single-triplet energy difference ΔE at magnetic field $B = 0$ shown in Fig. 2c with red curve. We discover a similar sensitive nature of ΔE due to the detuning, but the value flattens considerably after $\Delta V = 50$ meV suggesting further detuning has very little impact on the system.

A better understanding can be gained by examining the square root of electron densities calculated using Eq. (6) as plotted in Fig. 3 to give insight on the wavefunction. The square root densities of the singlet and the triplet state are plotted at zero magnetic field for detuning values $\Delta V = 0$ meV, $\Delta V = 46$ meV and $\Delta V = 60$ meV. It is crucial to note the fact that for a symmetric phosphorene dot system where the depth of dots is 60 meV a detuning of about even 10 meV renders very little change in the S/T energy difference. This robustness against detuning can be attributed to the large effective mass of the electrons, which leads to strong localization and electron-electron interaction[68]. For a symmetric system [Fig. 3a,b], the singlet and triplet states look very similar, with two electrons occupying both dots. The difference between square root density in between the two dots near $x = 0$ nm exhibit the bonding nature of the singlet state and the anti-bonding nature of the triplet state for $\Delta V = 0$. For $\Delta V = 46$ meV we see a different character of the singlet [3c] state. While the triplet state [3d] maintains similarity to the $\Delta V = 0$ case but with unequal occupation in the dots, the singlet state shows that almost both electrons occupy a single dot. The triplet state consists of two electrons with the same individual spin orientations. Due to the Pauli exclusion principle they cannot occupy a single dot with the same single electron energy states, responsible for blocking of transport through the dots, i.e. Pauli spin blockade[19,20] which was first reported in Ref.[69]. Whereas the singlet electrons can occupy a single dot where both electrons are in the lowest single electron energy levels with just the Coulomb repulsion and tunnel barrier to overcome. Hence, the steeper slope of the curves in Fig. 2b,c are due to significant density changes in the ground state and first excited state with respect to ΔV. Once the detuning becomes sufficiently large at $\Delta V = 60$ meV, both electrons occupy mostly the left dot and a further increase of detuning only increases the strength of confinement of the electrons.

Given the focus of this study is on spin-flip transitions, it is important to investigate the matrix element $\langle 1|x_1 + x_2|2\rangle$ since for a given field amplitude F and frequency ν, the transition probability is upper bounded by the value of this matrix element. Fig. 2c shows the transition matrix element (black curve) as a function of the detuning ΔV. For the symmetric system the Hamiltonian commutes with a generalized parity operator $\Pi = \Pi_1(1) \otimes \Pi_1(2)$, where Π_1 is the single-electron operator

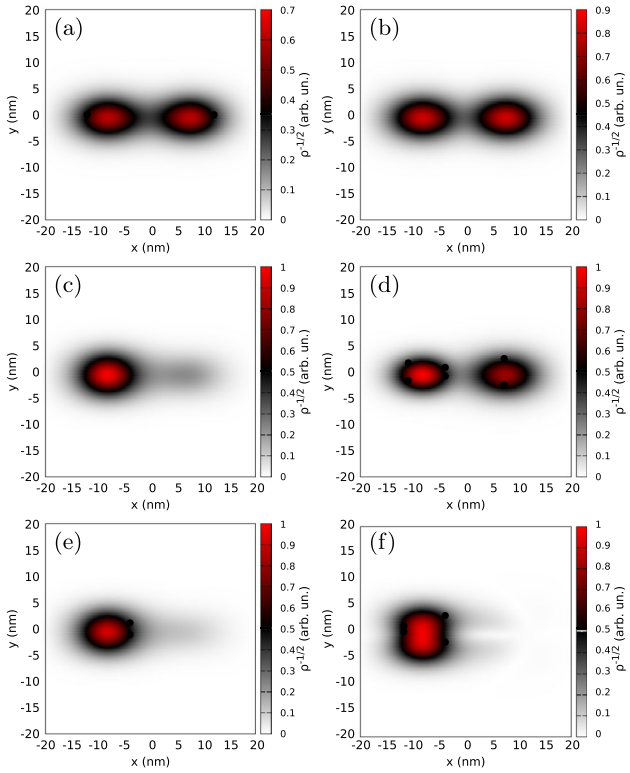

Figure 3. The square root of the charge density for the singlet (**a**,**c**,**e**) and the triplet (**b**,**d**,**f**) at $B = 0$ for a symmetric double dot system (**a**,**b**), $\Delta V = 46$ meV (**c**,**d**) and $\Delta V = 60$ meV (**e**,**f**).

$$\Pi_1 = \begin{pmatrix} P & 0 \\ 0 & -P \end{pmatrix}, \tag{8}$$

and P is the scalar parity operator $Pf(x, y) = Pf(-x, -y)$. For a symmetric potential the spin-up and spin-down components of the single-electron Hamiltonian wave functions have opposite parities. For two electrons, both the lowest-energy singlet and the lowest-energy triplet state with spin component $S_z = -\hbar$ correspond to negative eigenvalue of the Π operator. Due to the parity symmetry the transition dipole matrix elements $\langle n|x_1 + x_2|m\rangle$ vanish for states n, m corresponding to the same Π eigenvalue ± 1. This selection rule eliminates the possibility of a direct transition from singlet to the lowest triplet in the symmetric system as seen in Fig. 2c at $\Delta V = 0$, the value of matrix element is zero. The matrix element achieves its maximum value of 5.23 nm at $\Delta V = 46$ meV where the singlet has a charge state (2, 0) and the triplet with extended densities and charge state nearly (1, 1). This higher value of the transition matrix element is where we expect the largest chance in spin-flip transitions. Further beyond this point, the transition matrix reduces to lower values as the charge states for both states become the same, i.e. (2, 0).

The energy spectrum for the detuning $\Delta V = 1$ meV and $\Delta V = 46$ meV are presented in Fig. 4a and b respectively. In addition, the transition matrix element and the average $\langle S_z \rangle$ values are depicted in Fig. 4c and d. We observe that the avoided crossing is shifted to higher magnetic fields for the stronger detuning case just above 17 T, whereas for $\Delta V = 1$ meV, the S/T avoided crossing occurs at 0.545 T. At these points the transition matrix element is the largest. Although non-zero, the transition matrix element for weak asymmetry is three orders of magnitude smaller than for the other case. We also see the exchange of the $\langle S_z \rangle$ values at the avoided crossings as seen in the second row of the figure by the red and blue curves. The most desirable region in the spectrum for fast electrical control of the spin is near these S/T avoided crossings. There have been EDSR experiments[59–66] where the frequency of microwave radiation or the AC frequency of voltages on the gates is of order of few to 10 GHz, which corresponds to energies of order 0.0414 meV. We shall now examine the spin-flip transitions near these S/T avoided crossings, where the energy differences exhibit comparable magnitudes, making the results more relevant to experimental observations. In the following two sections we present the analysis with the external time-dependent electric field for the two cases of a small and large potential asymmetry shown in Fig. 4.

Spin-flip transitions

We first consider the case with the largest transition matrix element, i.e. for $\Delta V = 46$ meV. For such large asymmetry, as seen in the previous section, the spin singlet and triplet states are coupled with different charge states (1, 1) and (0, 2). The applied time-dependent electric field drives the system through spin orbit coupling. Using Eq. (7), the states were evolved typically for 20 ns for the plots presenting maximal occupation of spin flipped

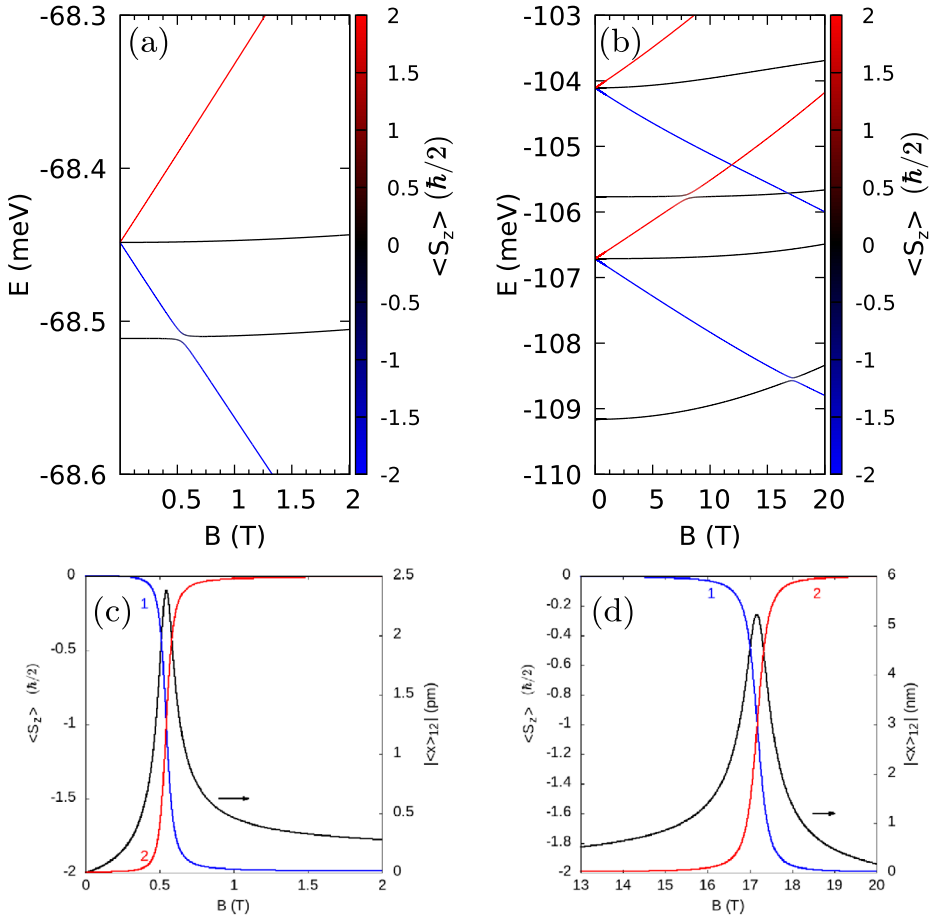

Figure 4. Two-electron energy spectrum for the double quantum dot system aligned with the x axis for asymmetry of the potential depth of (**a**) $\Delta V = 1$ meV and (**b**) $\Delta V = 46$ meV. The average $\langle S_z \rangle$ of the two lowest-energy levels referred to the left axis of (**c**) $\Delta V = 1$ meV and (**d**) $\Delta V = 46$ meV. Blue (Red) curves shows $\langle S_z \rangle$ value for ground (first excited) state. In (**c**) and (**d**) the black curve shows the dipole matrix element $\langle 1|x_1 + x_2|2\rangle$ between the ground state and the first excited state referred to the right axis.

states as functions of $h\nu$. Even larger simulation times are used for evaluation of the spin-flip time when it exceeds 20ns. The calculations are performed for magnetic field 16 T near the S/T avoided crossing. Fig. 5a shows maximal occupation in the first excited state max $|c_2|^2 = p_f$ (the targeted final state) found during 20ns simulation time as a function of frequency of the applied field. We plot the resonance spectrum for three field amplitudes F and for each field strength. Notice the two peaks corresponding to first and second order transitions from singlet to triplet. The direct transition occurs near the S/T energy difference ΔE of about 0.14 meV, while the second order transition occurs at half this value. Similar harmonic resonances were observed in experiments in GaAs double QD[61] and in GaAs heterostructures[9] in InAs nanowire double QD[70]. As the field strength increases, the peaks become broader with the second order transition always being sharper than the direct transition. Despite the increasing amplitudes, the positions of the peaks remain unchanged for both orders. This second order transition can be considered as two-photon transitions mediated by a virtual state. First the system undergoes an energy non-conserving transition to state $|m\rangle$ with the maximum probability determined by the transition matrix element x_{1m} and then from state $|m\rangle$ to state $|2\rangle$ with transition matrix element x_{m2}. The energy is conserved overall over the two transitions. Along with the matrix element, the contribution from each state of the system is inversely proportional to $[(\omega_{1m} - \omega)(\omega_{12} - 2\omega)]$. A much rigorous understanding can be obtained from the equations derived for the perturbative expansion of coefficients in Appendix A, which describes every feature of the peaks. This driving amplitude can be considered as weak since at $B = 16$T the matrix element of $\langle x_{12} \rangle = 1.59$ nm leads to $\frac{eF\langle x_{12}\rangle}{h\nu_{12}} \ll 1$. Due to a low amplitude of the driving field, no significant Bloch-Siegert shift[71] is observed in the resonance frequencies as seen from the figure. Note that the peaks in Fig. 5a are not visibly shifted when the amplitude of the driving field is altered.

At the resonance, time taken for spin-flip transition is plotted in Fig. 5b. Remarkably, even for amplitudes as small as 1 μV/nm, the spin-flip times remain close to 1 ns for the direct transitions. Whereas for the second order, a nano-second spin-flip occurs at amplitudes larger than 3.8 μV/nm. The second order transition times decrease as a function of $\frac{0.003872^2}{F^2}$ ns (nm/mV)^2, while the direct transition goes as $\frac{0.00105}{F}$ ns nm/mV. It is even possible to achieve a sub nano-second spin-flip time as we approach the field strength of 10 μV/nm. For even

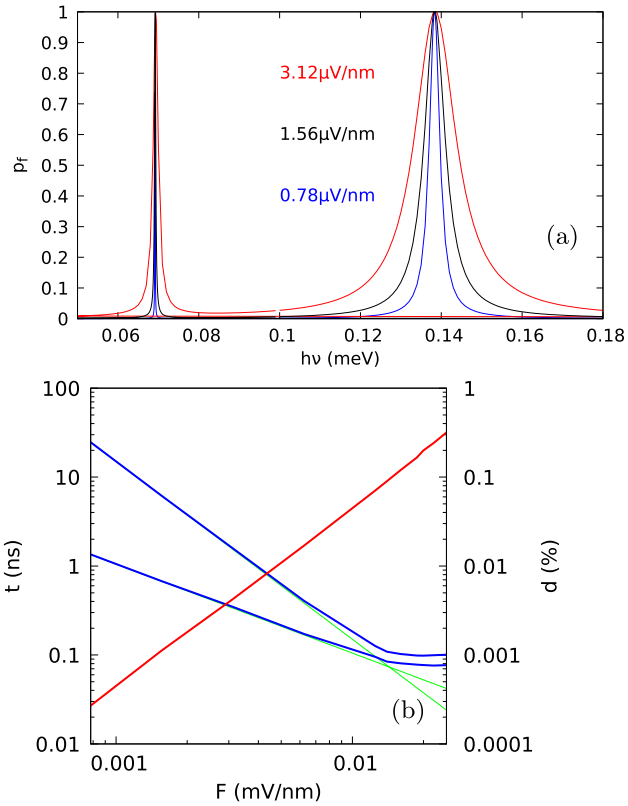

Figure 5. For $\Delta V = 46$ meV at magnetic field $B = 16$ T, (**a**) The maximal occupation of the triplet state for the time-dependent evolution of the system subject to the AC electric field with the amplitude of 0.78μV/nm (blue curve), 1.56μV/nm (black curve), and 3.12μV/nm (red curve) found in a simulation lasting 20 ns. (**b**) Blue solid and dashed lines show the singlet-triplet transition times as a function of the AC electric field amplitude for the first-order and second-order transitions, respectively. The two green thin lines show the linear and quadratic fits to the transition times vs the amplitude. The red line shows the contribution of the second and higher energy levels as a function of the AC field with slope of 2.

larger amplitudes, the lines lose their predicted dependence and deviate from the linear nature in the plot above $8\ \mu$V/nm . This occurs due to the leakage of the system into higher energy states. Maximal leakage of probability into higher states as depicted with the red line in Fig. 5b. This leakage can be calculated with the formula $d = 1 - (|c_1(t)|^2 + |c_2(t)|^2)$. When the leakage tends to zero, the system approaches an ideal two-level system, desirable for qubit applications and with dynamics accurately described by the Rabi model. We notice that even in the sub nano-second regime of the transitions, leakage is as low as 0.002% and grows quadratically with field amplitude F. A low leakage of the qubit is favoured to obtain norm conserving rotations on the Bloch sphere, which in turn is beneficial for higher gate fidelity and lower noise.

Such sub nanosecond transition between the two states of a qubit is reported often in charge qubits where the driving field is pulsed instead of sinusoidal, but it is still periodic[72–74]. This system can thus be used for fast sub-nanosecond spin manipulation operations without the practical intricacy of pulse generation and while retaining long coherence times due to weak spin-orbit coupling of phosphorene. These type of qubits are advantageous because of their quick operations, but they are also very vulnerable to material defects and charge noise from the quantum dot environment. The configuration described earlier with detuning of $\Delta V = 46$ meV can be regarded as a qubit where the spin and charge are strongly linked. It is possible to modify and tune this coupling via changing the original detuning, as shown in Fig. 2c. Weak coupling of the spin moment to the environment gives the advantage over a charge qubit in terms of large coherence times. A more spin-qubit like character can be obtained from the same setup by going to the other extreme end of detuning, i.e. a nearly symmetric system.

A similar analysis was therefore performed for $\Delta V = 1$ meV and maximum of occupation $|c_2|^2$ with respect to the AC frequency of the electric field ν was obtained. Results for various electric field amplitudes are shown in Fig. 6. The magnetic field near the avoided crossing of 0.4 T and 0.9 T are chosen, the energy difference and its first few fractions are listed in Table 1. The simulation starts from the ground state, i.e. the singlet state for magnetic field 0.4 T and the triplet state for magnetic field 0.9 T. Immediately, we observe that despite the significantly smaller S/T energy difference in this scenario compared to the previous one, a much higher field is needed to induce the transition within the simulation time. This is because of the transition matrix elements being three orders of magnitude lower now [see Fig. 4c and d]. An amplitude $F = 0.2$ mV/nm of the electric field produces a resonance spectrum as shown in the bottom part of Fig. 6a (for $B = 0.4$ T) and of Fig. 6b (for $B = 0.9$

B (T)	ΔE_{12} (meV)	$\frac{\Delta E_{12}}{2}$ (meV)	$\frac{\Delta E_{12}}{3}$ (meV)	$\langle x_{12} \rangle$ (pm)
0.4	0.017232	0.0086160	0.0057440	0.593
0.9	0.042037	0.0210185	0.0140123	0.531

Table 1. Energy difference and transition matrix element between singlet and triplet states near the avoided crossing for detuning $\Delta V = 1$ meV.

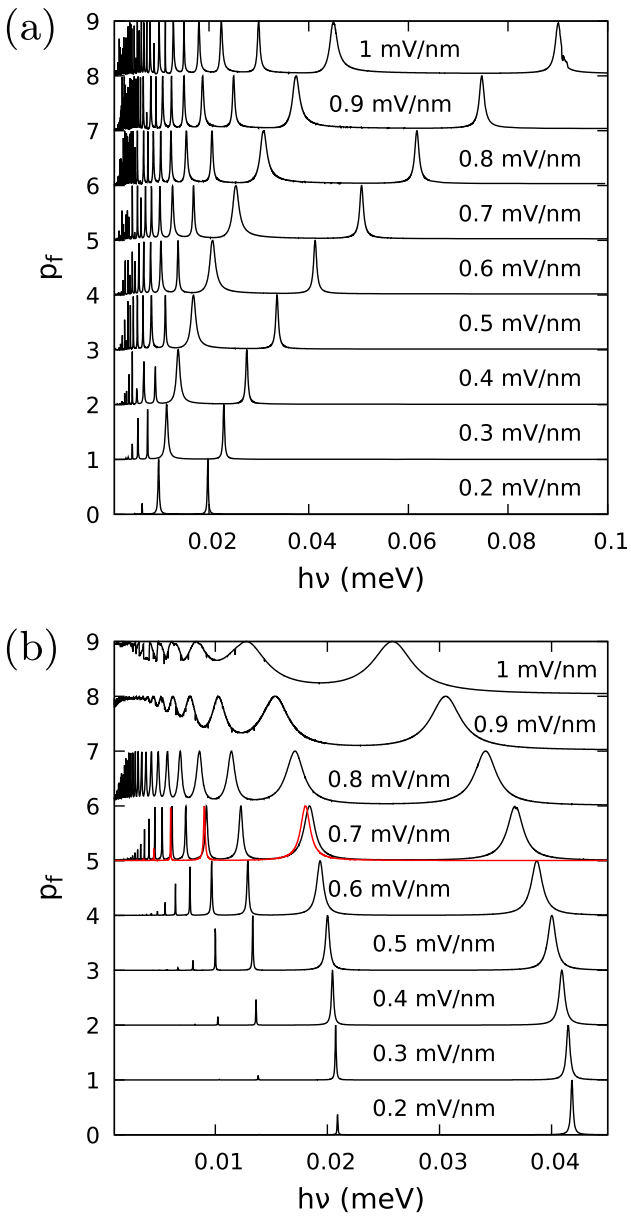

Figure 6. Maximal occupation of the first excited state calculated similar to Fig. 5 for $\Delta V = 1$ meV in the external magnetic field of (**a**) 0.4 T and (**b**) 0.9 T. The plots for an increasing amplitude of the AC field are shifted by 1 in panels (**a**) and (**b**). The red curve in panel (**b**) shows the results for an ideally symmetric double dot and the amplitude of $F = 0.7$ mV/nm with presence of only even order transitions. The simulation time in both the plots is set to 20 ns.

T). We detect resonances occurring near frequencies where the corresponding energies match the energy differences and their fractions. First resonance peak from the right corresponds to a direct spin-flip transition where $h\nu \approx \Delta E_{12}$. At the peak, we find that the direct spin-flip time is above 12 ns. The second peak from the right is the second order transition where $h\nu \approx \Delta E_{12}/2$. Higher order transitions can be explained using expansion of the coefficients $c_i(t)$ and recursively solving for higher orders of the coefficients (cf. Appendix A). The nth order

transition (or n-photon transition) coefficient is proportional to $(eF/2\hbar)^n$. Thus, as the amplitudes get larger, the peak heights of higher order resonances grow one order of F faster. The transition rates for the higher order resonances can further be increased by tuning the interdot tunnel barrier[75].

The resonance spectra for higher amplitudes of the electric fields are shifted by one along the y-axis in the plot. We see that resonance peaks blue-shift as a result of higher amplitudes before the S/T avoided crossing where the initial state is singlet [Fig. 6a]. On the contrary even with similar size of the transition matrix elements (Table 1), the resonance peaks red-shift to lower energies with increasing amplitude of the electric field after the crossing ($B = 0.9$ T) when the initial state is the triplet [See Fig. 6b]. Here as well, the higher order peaks occur with increasing amplitude, which agrees well with the energy differences for lower amplitudes of field. But at amplitudes higher than 0.7 mV/nm, at lower frequencies, the occupancy is no longer zero and for amplitudes more than 0.9 mV/nm, the occupancy is almost one. This corresponds to the adiabatic triplet to singlet transitions governed by the Landau-Zener-Stückelberg-Majorana (LZSM) formula[42,43]. Such adiabatic transition only occurs for the case when the triplet is the ground state due to singlet state being pushed down as a result of the asymmetry created by the electric field. Fig. 7a shows the lowest four energy levels as a function of constant electric field with the singlet as the ground state. We observe that the field pushes the singlet state down for large values of 1 mV/nm or −1 mV/nm. Similar behaviour is seen in Fig. 7b for $B = 0.9$ T except we see an avoided crossing at about 0.76 mV/nm. Thus for small frequency of electric field, the state sweeps adiabatically from triplet to singlet causing the spin flip transition. LZSM mechanism was also reported to induce the multiple harmonic generation in multilevel systems[76]. For a perfectly symmetric system, the resonance spectrum is shown in Fig. 6b by the red curve. Clearly showing the absence of the direct transition, as well as the absence of the higher peaks of odd n-order due to the parity selection rule.

The higher amplitude required to drive the transitions indicates that such a system where the charge states are not strongly linked with spin states will be more robust against the external charge noise and material defects. As we notice from Fig. 2c, a detuning of even 10 meV will keep the system more or less the same, with the transition matrix element as well as the avoided crossing vary by smaller amount as compared to the previous case. A trade-off of this extreme being weak coupling to the external electric field which influences the transition times.

Spin-flip times of the nearly symmetric system before and after the S/T avoided crossing are shown in Fig. 8. The solid (dotted) lines indicate the first (second) order transition times. For even amplitudes 10 to 100 times larger than the previous case, spin-flip times are about 80 ns. Spin-flip time at $B = 0.9$ T for direct transitions is similar to that of $B = 0.4$ T case for lower amplitudes. However, once the amplitude exceeds 0.2 mV/nm and the peaks red-shift, the triplet transitions to singlet state are more rapid compared to the reverse transition. The second order transitions, even though slower than direct transitions for lower amplitudes, become much faster than the direct transitions and follow the trend of $1/F^2$. Whereas the direct transitions evolve proportional to $1/F$. This proportionality breaks down as the amplitude approaches 1 mV/nm and contribution from higher states reaches up to 4%. These amplitudes can then drive the spin-flip transitions at sub nano-second scale, but the fidelity of such operations would be very low because of leakage.

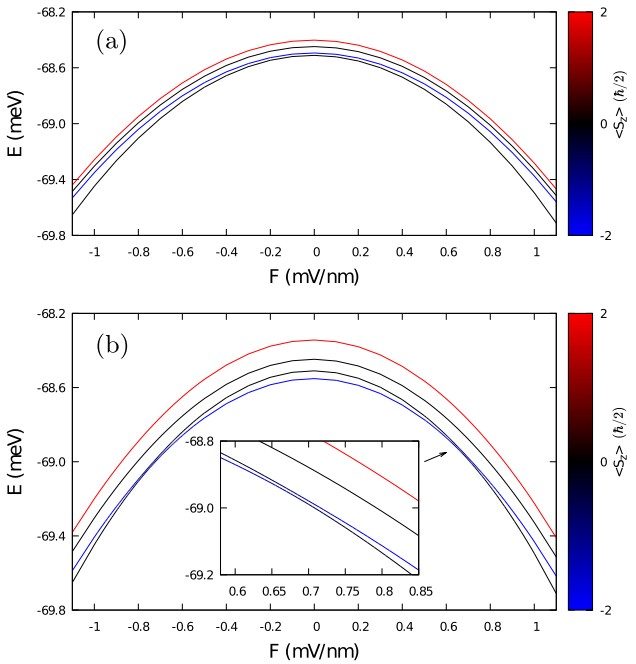

Figure 7. For $\Delta V = 1$ meV at magnetic field (**a**) $B = 0.4$ T and (**b**) $B = 0.9$ T. Energy levels as function of constant electric field perturbation showing the avoided crossing in (**b**) for $B = 0.9$ T which is shown more clearly in the inset figure.

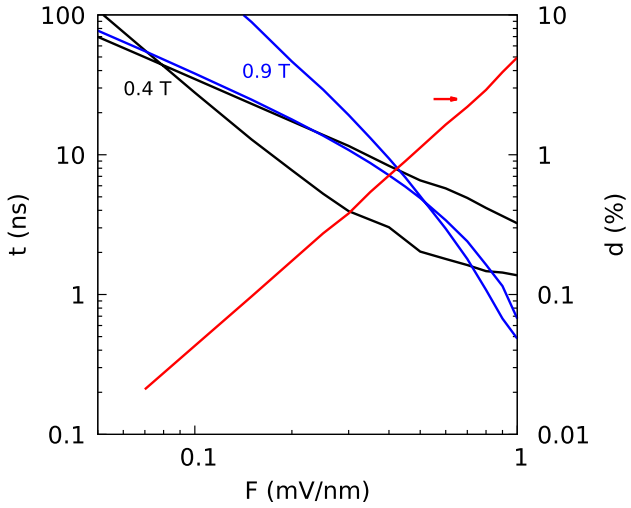

Figure 8. Same as Fig. 5b but for $\Delta V = 1$meV. The black and blue lines correspond to $B = 0.4$ T (Fig. 4(a)) and $B = 0.9$ T [cf. Fig. 6b], respectively.

Dots arranged in the zig-zag direction

Weaker inter-dot coupling can be achieved by arranging the dots in the y-direction within the same material and geometric parameters. By modifying Eq. (3) so that the center of Gaussians are at $y = \pm d$ and changing the electric field to be $V'(t) = -eFy\Theta(t)\sin(\omega t)$, we can investigate the effects of asymmetry and spin-flip transitions analogous to previous sections and compare the results for a different inter-dot coupling.

Figure 9a and b show the energy spectrum for the dots arranged vertically at the detuning $\Delta V = 42$ meV and $\Delta V = 46$ meV, respectively. We see similar features as seen for dots arranged in x-direction. The ground state is a singlet and is replaced by the triplet after the avoided crossing. It occurs for a very small value as compared to the previous cases, with the center of avoided crossing for $\Delta V = 42$ meV at about 50 mT. Which is in contrast to the dots in x-direction, where the detuning of about $\Delta V = 42$ meV moved the center of avoided crossing above 5 T. At $\Delta V = 45$ meV, the position of avoided crossing has reached about 5.5 T. Due to the lower tunneling coupling between the dots, the slope of the position of avoided crossing [see Fig. 9c] is much steeper. It occurs at very low values for up to $\Delta V = 42$ meV and then shoots up to values more than 10 T before ΔV even reaches 50 meV. This sensitivity to the detuning is also reflected in the transition matrix and S/T energy gaps in Fig. 9d. The transition matrix element between singlet-triplet achieves its maximum at 45 meV with values of about 7 nm. Because of the strong electron-electron interaction in y-direction, detuning of about 35 meV has basically no effect on the S/T energy difference and the transition matrix, meaning the densities are largely unaffected. The square root densities of the lowest singlet and triplet of this system for symmetric, $\Delta V = 45$ meV and $\Delta V = 50$ meV are plotted in Fig. 10. Note the smaller values of square root densities between the dots [see Figs. 10a,b], indicating a much weaker inter-dot coupling compared to Fig. 4a,b for symmetric dots arrange in x-direction. The effect of this is also seen for the case where transition matrix element is the largest. The square root density of singlet [Fig. 10c] shows both electrons completely occupied in the bottom dot with almost no leakage to the other dot because of weak tunneling, contrary to singlet in Fig. 4c. With the large enough detuning [Fig. 9e,f], both the triplet states electrons eventually occupy the lower dot. Once the electrons have both occupied the lower dot, the position of avoided crossing and the S/T energy difference saturates similar to the situation in the earlier sections.

We now focus the case with the largest transition matrix element, i.e. for $\Delta V = 45$ meV. An analysis similar to that of horizontal dots was performed to obtain the spin-flip times illustrated in Fig. 11. The magnetic field was chosen to be 4.5 T near the avoided crossing in Fig. 9b where the electric field drives the system from the ground state singlet to the spin polarized triplet. At the field amplitude of 2 μV/nm, we see that the spin flip time is 2.875 ns, whereas due to stronger coupling and tunneling, spin flip time for dots in horizontal orientation at this amplitude was already 0.525 ns [cf. Fig. 5b]. A sub-nanosecond spin-flip occurs for amplitudes great than 5.75 μV/nm. The first and second order transitions follow a similar trend, the first order transition time reduces as $\frac{0.00575}{F}$ ns nm/mV and the second order as $\frac{0.00866^2}{F^2}$ ns $(\text{nm/mV})^2$ resulting in a second-order nanosecond spin-flip at an amplitude of 8.6 μV/nm. Although the sub-nanosecond spin manipulation is possible in this case, cost of it is paid in the leakage due to higher amplitudes. A half nano-second spin-flip occurs with leakage of about 0.005% for dots with stronger inter-dot coupling (dots in x-direction) while for dots with weaker coupling the same spin-flip time is not observed as a consequence of leakage to higher states. The contribution of higher energy states is shown in red referred to the right axis in Fig. 11. Higher amplitudes increase the contribution of higher states, with the trend being quadratic for lower amplitudes. The leakage grows rapidly to about 2% as the amplitude approaches 30 μV/nm. When the contribution of the higher state reaches about 0.05%, transition time lines deviate away from linear and quadratic fits.

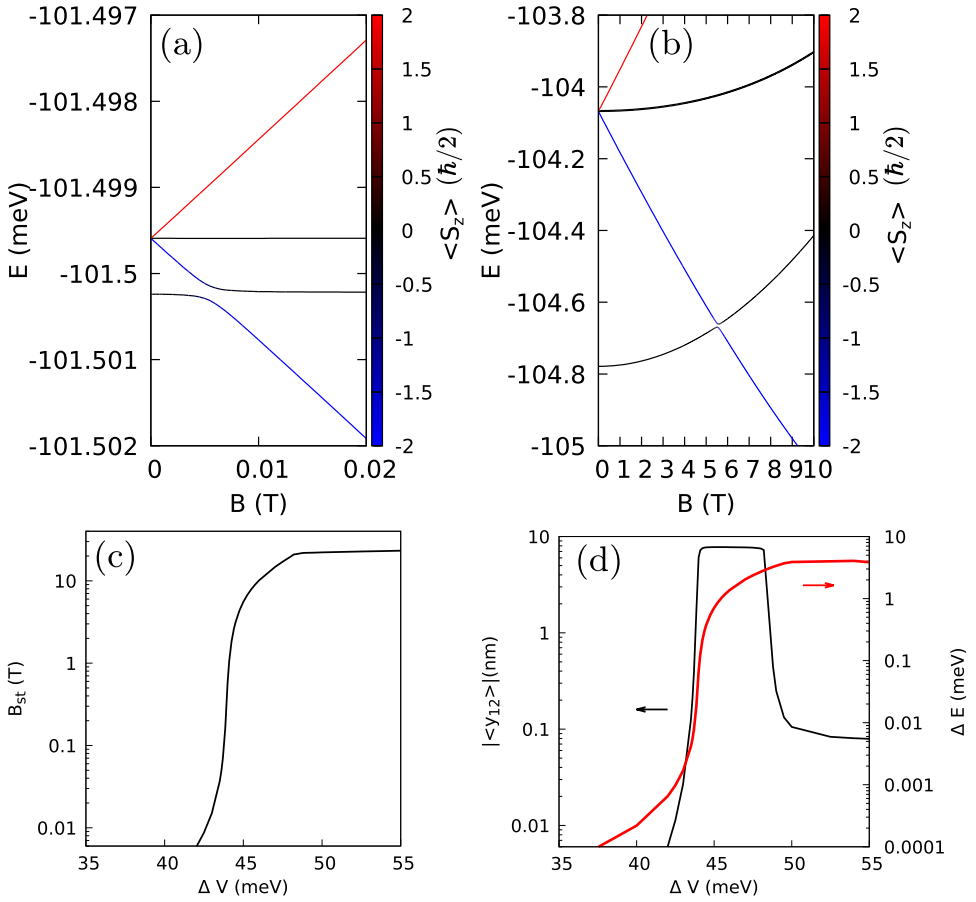

Figure 9. The energy spectrum for (**a**) $\Delta V = 42$ meV and (**b**) $\Delta V = 45$ meV. (**c**) The magnetic field position of the singlet-triplet avoided crossing vs ΔV. The field is basically zero unless both the electrons in the singlet drop in the deeper dot. (**d**) The maximal value of the transition matrix element (black curve) for the S/T transition referred to left axis and the exchange energy (red curve) at $B = 0$ referred to the right axis.

Summary and conclusions

We presented an analysis of the singlet-triplet energy splitting and singlet-triplet transitions driven by oscillating electric field in double quantum dots with the effective mass and spin-orbit coupling anisotropy in phosphorene using an exact numerical treatment involving configuration interaction method and the two-electron eigenstates used as a basis for integrating the time evolution of the driven system. The potential asymmetry and orientation of the confinement potential was discussed. The first order singlet-triplet transition turns out to be forbidden by the parity symmetry selection rules in symmetric system of quantum dots. The dipole matrix element for the transition depends strongly on the asymmetry of the confinement potential in a non-monotonic way, with a maximum corresponding to an asymmetry which localizes the singlet in one of the quantum dots and the triplet state still extended over both the dots.

We studied the times of the resonant spin flips including the first and higher-order transitions and the fidelity of the flip versus the amplitude of the driving electric field. Fast sub-nanosecond singlet-triplet transitions involving only the initial and final states are easily achieved for anisotropic quantum dots arranged in the armchair direction. This is possible due to the strong electron-electron interaction in the phosphorene. Detuning can be used to control the sensitivity to charge noise and increase fidelity of operation while simply using the oscillating driving without even employing optimization methods. For the quantum dots arranged in the zig-zag direction fast spin transition times are obtained only at the cost of the leakage of the two-electron wave function to higher excited energy levels. The advantage of using phosphorene for spin manipulation in gated double quantum dots is that the interdot coupling, the spin-transition times and the leakage of the states beyond the two lowest-energy states can be additionally controlled by orientation of the axis of the double dot system with respect to the crystalographic axes of the 2D crystal.

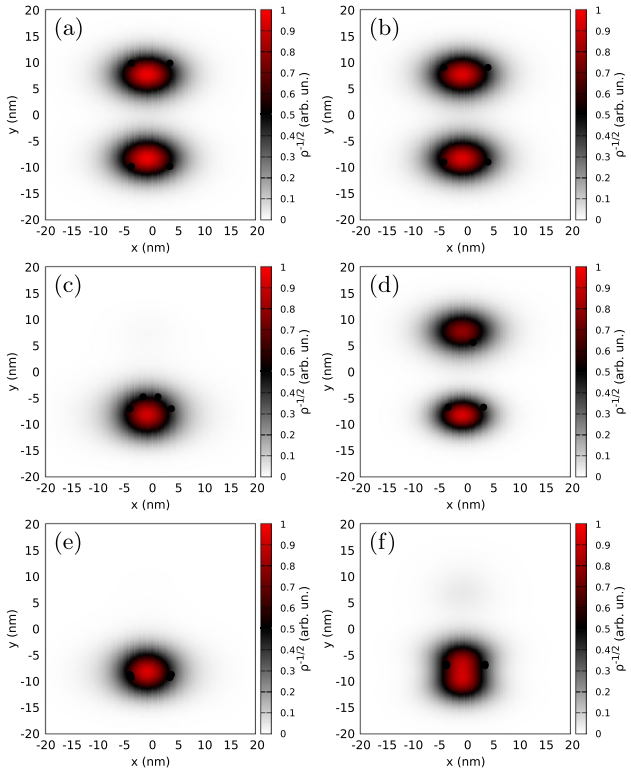

Figure 10. A square root of the electron density for a symmetric double dot system (**a**,**b**), $\Delta V = 45$ meV (**c**,**d**) and $\Delta V = 50$ meV (**e**,**f**). The left panel (**a**,**c**,**e**) shows the lowest singlet state and the right panel (**b**,**d**,**f**) the lowest triplet state. The results were calculated for $B = 0$.

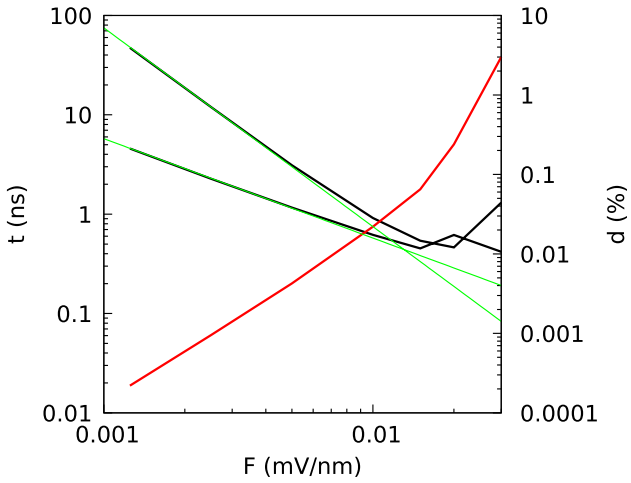

Figure 11. Same as Fig. 5b but for dots arranged in zig-zag direction with $\Delta V = 45$ meV at $B = 4.5$ T. The black solid (dashed) line indicates spin-flip time for first (second) order transitions. Green lines show the linear and quadratic fits.

For lower asymmetry of the confinement potential with both the singlet and the triplet states extended the dipole matrix element is by order magnitudes smaller than its optimal value and the singlet-triplet transition times of the order of several ns are obtained only at high amplitude of the driving field which is accompanied by a series of subharmonic resonances and Landau-Zener transitions at low frequencies driving the system across the singlet-triplet avoided crossings.

Data availability

The datasets used and/or analysed during the current study available from the corresponding author on reasonable request.

Expansion of coefficients

The coefficients for any n-level system in Eq. (7) can be solved using perturbative expansion,

$$c_n(t) = c_n^{(0)}(t) + c_n^{(1)}(t) + c_n^{(2)}(t) + \ldots, \tag{A1}$$

where zeroth order simply being the initial condition. Subsequent orders of expansion can be obtained by substituting previous order in the right hand side of Eq. (7). Without using the rotating-wave approximation (RWA) we obtain the expressions for the coefficients by integrating up to time t as

$$\begin{aligned}
c_n^{(1)}(t) &= \frac{eFx_{1n}}{2i\hbar}\cdot \\
&\quad \left\{\frac{1-\exp[i(\nu_{1n}+\nu)t]}{\nu_{1n}+\nu} + \frac{1-\exp[i(\nu_{1n}-\nu)t]}{\nu_{1n}-\nu}\right\} \\
c_n^{(2)}(t) &= -\left(\frac{eF}{2i\hbar}\right)^2 \cdot \sum_m x_{mn}\, x_{1m} \\
&\quad \left\{\frac{1-\exp[i(\nu_{mn}+\nu)t]}{(\nu_{mn}+\nu)(\nu_{1m}+\nu)} - \frac{1-\exp[i(\nu_{mn}+\nu_{1m}+2\nu)t]}{(\nu_{1m}+\nu)(\nu_{mn}+\nu_{1m}+2\nu)}\right. \\
&\quad + \frac{1-\exp[i(\nu_{mn}+\nu)t]}{(\nu_{mn}+\nu)(\nu_{1m}-\nu)} - \frac{1-\exp[i(\nu_{mn}+\nu_{1m})t]}{(\nu_{1m}-\nu)(\nu_{mn}+\nu_{1m})} \\
&\quad - \frac{1-\exp[i(\nu_{mn}-\nu)t]}{(\nu_{mn}-\nu)(\nu_{1m}+\nu)} + \frac{1-\exp[i(\nu_{mn}+\nu_{1m})t]}{(\nu_{1m}-\nu)(\nu_{mn}+\nu_{1m})} \\
&\quad \left. - \frac{1-\exp[i(\nu_{mn}-\nu)t]}{(\nu_{mn}-\nu)(\nu_{1m}-\nu)} + \frac{1-\exp[i(\nu_{mn}+\nu_{1m}-2\nu)t]}{(\nu_{1m}-\nu)(\nu_{mn}+\nu_{1m}-2\nu)}\right\}
\end{aligned} \tag{A2}$$

where x_{mn} is the matrix element $\langle m|x|n\rangle$ and $\nu_{mn} = (E_m - E_n)/h$. We can obtain a much convenient form of these expressions under RWA by removing fast moving components as,

$$\begin{aligned}
c_n^{(1)}(t) &= \frac{eF}{2i\hbar}\, x_{1n}\, \frac{\exp[it(\nu_{1n}-\nu)/2]\sin(it(\nu_{1n}-\nu)/2)}{(\nu_{1m}-\nu)} \\
c_n^{(2)}(t) &= \left(\frac{eF}{2i\hbar}\right)^2 \sum_m x_{1m}\, x_{mn} \\
&\quad \cdot\left\{\frac{\exp[it(\nu_{mn}-\nu)/2]\sin(it(\nu_{mn}-\nu)/2)}{(\nu_{mn}-\nu)(\nu_{1m}-\nu)}\right. \\
&\quad \left. + \frac{\exp[it(\nu_{mn}+\nu_{1m}-2\nu)/2]\sin(it(\nu_{mn}+\nu_{1m}-2\nu)/2)}{(\nu_{1m}-\nu)(\nu_{1m}+\nu_{mn}-2\nu)}\right\}
\end{aligned} \tag{A3}$$

The coefficients reach their maximum when the arguments of sine function tend to zero. The absolute values of nth order coefficient is proportional to nth power of F, thus nth order transition times will be proportional to $1/F^n$.

Received: 6 June 2024; Accepted: 17 July 2024
Published online: 16 August 2024

References

1. Atherton, N. M. *Electron Spin Resonance: Theory and Applications* (Halsted Press, 1973).
2. Engel, H. A. & Loss, D. Single-spin dynamics and decoherence in a quantum dot via charge transport. *Phys. Rev. B* **65**, 195321 (2002).
3. Koppens, F. H. *et al.* Driven coherent oscillations of a single electron spin in a quantum dot. *Nature* **442**(7104), 766–771 (2006).
4. Wolf, S. A. *et al.* Spintronics: A spin-based electronics vision for the future. *Science* **294**(5546), 1488–1495 (2001).
5. Awschalom, D. & Loss, D. *Semiconductor Spintronics and Quantum Computation* (Springer Science & Business Media, 2002).
6. Hanson, R., Kouwenhoven, L. P., Petta, J. R., Tarucha, S. & Vandersypen, L. M. Spins in few-electron quantum dots. *Rev. Mod. Phys.* **79**(4), 1217 (2007).
7. Loss, D. & DiVincenzo, D. P. Quantum computation with quantum dots. *Phys. Rev. A* **57**(1), 120 (1998).
8. Burkard, G., Loss, D. & DiVincenzo, D. P. Coupled quantum dots as quantum gates. *Phys. Rev. B* **59**(3), 2070 (1999).
9. Forster, F., Mühlbacher, M., Schuh, D., Wegscheider, W. & Ludwig, S. Electric-dipole-induced spin resonance in a lateral double quantum dot incorporating two single-domain nanomagnets. *Phys. Rev. B* **91**(19), 195417 (2015).
10. Yoneda, J. *et al.* Fast electrical control of single electron spins in quantum dots with vanishing influence from nuclear spins. *Phys. Rev. Lett.* **113**(26), 267601 (2014).
11. Bell, R. L. Electric dipole spin transitions in InSb. *Phys. Rev. Lett.* **9**(2), 52 (1962).
12. Golovach, V. N., Borhani, M. & Loss, D. Electric-dipole-induced spin resonance in quantum dots. *Phys. Rev. B* **74**(16), 165319 (2006).
13. Bemski, G. Spin resonance of conduction electrons in InSb. *Phys. Rev. Lett.* **b**(2), 62 (1960).
14. Meier, L. *et al.* Measurement of Rashba and Dresselhaus spin-orbit magnetic fields. *Nat. Phys.* **3**(9), 650–654 (2007).

15. Rashba, E. I. & Efros, A. L. Orbital mechanisms of electron-spin manipulation by an electric field. *Phys. Rev. Lett.* **91**(12), 126405 (2003).
16. Reiner, J. *et al.* High-fidelity initialization and control of electron and nuclear spins in a four-qubit register. *Nat. Nanotech.* **1**, 1–7 (2024).
17. Froning, F. N. Ultrafast hole spin qubit with gate-tunable spin-orbit switch functionality. *Nat. Nanotech.* **16**(3), 308–312 (2021).
18. Takeda, K., Noiri, A., Yoneda, J., Nakajima, T. & Tarucha, S. Resonantly driven singlet-triplet spin qubit in silicon. *Phys. Rev. Lett.* **124**(11), 117701 (2020).
19. Hanson, R. & Awschalom, D. D. Coherent manipulation of single spins in semiconductors. *Nature* **453**(7198), 1043–1049 (2008).
20. Petta, J. R. *et al.* Coherent manipulation of coupled electron spins in semiconductor quantum dots. *Science* **309**(5744), 2180–2184 (2005).
21. Stepanenko, D., Rudner, M., Halperin, B. I. & Loss, D. Singlet-triplet splitting in double quantum dots due to spin-orbit and hyperfine interactions. *Phys. Rev. B* **85**(7), 075416 (2012).
22. Khomitsky, D. V., Gulyaev, L. V. & Sherman, E. Y. Spin dynamics in a strongly driven system: Very slow Rabi oscillations. *Phys. Rev. B* **85**(12), 125312 (2012).
23. Khomitsky, D. V., Lavrukhina, E. A. & Sherman, E. Y. Spin rotation by resonant electric field in few-level quantum dots: Floquet dynamics and tunneling. *Phys. Rev. Appl.* **14**(1), 014090 (2020).
24. Koppens, F. H. L., Nowack, K. C. & Vandersypen, L. M. K. Spin echo of a single electron spin in a quantum dot. *Phys. Rev. Lett.* **100**(23), 236802 (2008).
25. Nadj-Perge, S., Frolov, S. M., Bakkers, E. P. A. M. & Kouwenhoven, L. P. Spin-orbit qubit in a semiconductor nanowire. *Nature* **468**(7327), 1084–1087 (2010).
26. Van den Berg, J. W. G. *et al.* Fast spin-orbit qubit in an indium antimonide nanowire. *Phys. Rev. Lett.* **110**(6), 066806 (2013).
27. Liu, B. *et al.* Tuning the Schottky contacts in the phosphorene and graphene heterostructure by applying strain. *Phys. Chem. Chem. Phys.* **18**, 19918 (2016).
28. Stano, P. & Fabian, J. Orbital and spin relaxation in single and coupled quantum dots. *Phys. Rev. B* **74**, 045320 (2006).
29. Hofmann, A. *et al.* Anisotropy and suppression of spin-orbit interaction in a GaAs double quantum dot. *Phys. Rev. Lett.* **119**(17), 176807 (2017).
30. Scarlino, P. *et al.* Spin-relaxation anisotropy in a GaAs quantum dot. *Phys. Rev. Lett.* **113**(25), 256802 (2014).
31. Farzaneh, S. M. & Rakheja, S. Extrinsic spin-orbit coupling and spin relaxation in phosphorene. *Phys. Rev. B* **100**(24), 245429 (2019).
32. Popović, Z. S., Kurdestany, J. M. & Satpathy, S. Electronic structure and anisotropic Rashba spin-orbit coupling in monolayer black phosphorus. *Phys. Rev. B* **92**(3), 035135 (2015).
33. Low, T., Jiang, Y. & Guinea, F. Topological currents in black phosphorus with broken inversion symmetry. *Phys. Rev. B* **92**, 235447 (2015).
34. Liu, H. *et al.* Phosphorene: An unexplored 2D semiconductor with a high hole mobility. *ACS Nano* **8**(4), 4033–4041 (2014).
35. Long, G. *et al.* Achieving ultrahigh carrier mobility in two-dimensional hole gas of black phosphorus. *Nano Lett.* **16**(12), 7768–7773 (2016).
36. Long, G. *et al.* Ambipolar quantum transport in few-layer black phosphorus. *Phys. Rev. B* **96**(15), 155448 (2017).
37. Yang, J. *et al.* Integer and fractional quantum hall effect in ultrahigh quality few-layer black phosphorus transistors. *Nano Lett.* **18**(1), 229–234 (2018).
38. Derbali, S. & Moudam, O. Insights into the Application of 2D Phosphorene in Dye-Sensitized Solar Cells. *Energy Technol.* **11**(9), 2300353 (2023).
39. Schuster, R., Trinckauf, J., Habenicht, C., Knupfer, M. & Büchner, B. Anisotropic particle-hole excitations in black phosphorus. *Phys. Rev. Lett.* **115**(2), 026404 (2015).
40. Tian, X. *et al.* Recent advances in the development of nanomedicines for the treatment of ischemic stroke. *Bioact. Mater.* **6**(9), 2854–2869 (2021).
41. Sun, Z. *et al.* Ultrasmall black phosphorus quantum dots: synthesis and use as photothermal agents. *Angew. Chem. Int. Ed.* **54**(39), 11526–11530 (2015).
42. Ivakhnenko, V., Shevchenko, S. N. & Nori, F. Nonadiabatic Landau-Zener-Stückelberg-Majorana transitions, dynamics, and interference. *Phys. Rep.* **995**, 1–89 (2023).
43. Kofman, P. O., Ivakhnenko, O. V., Shevchenko, S. N. & Nori, F. Majorana's approach to nonadiabatic transitions validates the adiabatic-impulse approximation. *Sci. Rep.* **13**(1), 5053 (2023).
44. Szafran, B. Electrostatic quantum dot confinement in phosphorene. *Phys. Rev. B* **101**(23), 235313 (2020).
45. Faria Junior, P. E., Kurpas, M., Gmitra, M. & Fabian, J. k· p theory for phosphorene: Effective g-factors, Landau levels, and excitons. *Phys. Rev. B* **b**(11), 115203 (2019).
46. Zhou, X. *et al.* Effective g factor in black phosphorus thin films. *Phys. Rev. B* **95**(4), 045408 (2017).
47. Gillgren, N. *et al.* Gate tunable quantum oscillations in air-stable and high mobility few-layer phosphorene heterostructures. *2D Materials* **2**(1), 011001 (2014).
48. Li, L. *et al.* Quantum Hall effect in black phosphorus two-dimensional electron system. *Nat. Nanotech.* **11**(7), 593–597 (2016).
49. Yang, F. C Quantum hall effect in electron-doped black phosphorus field-effect transistors. *Nano Lett.* **18**(10), 6611–6616 (2018).
50. Thakur, T. & Szafran, B. Wigner molecules in phosphorene quantum dots. *Phys. Rev. B* **106**(20), 205304 (2022).
51. Thakur, T. & Szafran, B. Vortex structure in Wigner molecules. *Sci. Rep.* **13**(1), 9707 (2023).
52. Lis, K., Bednarek, S., Szafran, B. & Adamowski, J. Electrostatic quantum dots with designed shape of confinement potential. *Physica E* **17**, 494–497 (2003).
53. Chen, J., Wu, K., Hu, W. & Yang, J. Spin-orbit coupling in 2D semiconductors: A theoretical perspective. *J. Phys. Chem. Lett.* **12**(51), 12256 (2021).
54. Ho Park, Y. Separation of Rashba and Dresselhaus spin-orbit interactions using crystal direction dependent transport measurements. *Appl. Phys. Lett.* **103**(25), 252407 (2003).
55. Luo, J., Munekata, H., Fang, F. F. & Stiles, P. J. Effects of inversion asymmetry on electron energy band structures in GaSb/InAs/GaSb quantum wells. *Phys. Rev. B* **41**(11), 7685 (1990).
56. Nitta, J., Akazaki, T., Takayanagi, H. & Enoki, T. Gate control of spin-orbit interaction in an inverted $In_{0.53}Ga_{0.47}As/In_{0.52}Al_{0.48}$ as heterostructure. *Phys. Rev. Lett.* **78**(7), 1335 (1997).
57. Liang, D. & Gao, X. P. Strong tuning of Rashba spin-orbit interaction in single InAs nanowires. *Nano Lett.* **12**(6), 3263–3267 (2012).
58. Acosta, C. M., Ogoshi, E., Fazzio, A., Dalpian, G. M. & Zunger, A. The Rashba scale: Emergence of band anti-crossing as a design principle for materials with large rashba coefficient. *Matter* **3**(1), 145–165 (2020).
59. van der Wiel, W. G., Fujisawa, T., Tarucha, S. & Kouwenhoven, L. P. A double quantum dot as an artificial two-level system. *Jpn. J. Appl. Phys.* **40**(3S), 2100 (2001).
60. Forster, F. *et al.* Characterization of qubit dephasing by Landau-Zener-Stückelberg-Majorana interferometry. *Phys. Rev. Lett.* **112**(11), 116803 (2014).
61. Laird, E. A. *et al.* A new mechanism of electric dipole spin resonance: Hyperfine coupling in quantum dots. *Semicond. Sci. Technol.* **24**(6), 064004 (2009).

62. Nadj-Perge, S. *et al.* Spectroscopy of spin-orbit quantum bits in indium antimonide nanowires. *Phys. Rev. Lett.* **108**(16), 166801 (2012).
63. Corna, A. *et al.* Electrically driven electron spin resonance mediated by spin-valley-orbit coupling in a silicon quantum dot. *NPJ Quantum Information* **4**(1), 6 (2018).
64. Nowack, K. C., Koppens, F. H. L., Nazarov, Y. V. & Vandersypen, L. M. K. Coherent control of a single electron spin with electric fields. *Science* **318**(5855), 1430–1433 (2007).
65. Hu, R. Z. *et al.* Flopping-mode spin qubit in a Si-MOS quantum dot. *Appl. Phys. Lett.* **122**(13), 5 (2023).
66. Wagner, T. *et al.* Quantum stochastic resonance in an ac-driven single-electron quantum dot. *Nat. Phys.* **15**(4), 330–334 (2019).
67. Castelano, L. K. *et al.* Optimal control of universal quantum gates in a double quantum dot. *Phys. Rev. B* **97**(23), 235301 (2018).
68. Thakur, T. & Szafran, B. Nagaoka ferromagnetism in an array of phosphorene quantum dots. *Sci. Rep.* **13**(1), 18796 (2023).
69. Ono, K., Austing, D. G., Tokura, Y. & Tarucha, S. Current rectification by Pauli exclusion in a weakly coupled double quantum dot system. *Science* **297**(5585), 1313–1317 (2002).
70. Stehlik, J., Schroer, M. D., Maialle, M. Z., Degani, M. H. & Petta, J. R. Extreme harmonic generation in electrically driven spin resonance. *Phys. Rev. Lett.* **112**(22), 227601 (2014).
71. Romhanyi, J., Burkard, G. & Pályi, A. Subharmonic transitions and Bloch-Siegert shift in electrically driven spin resonance. *Phys. Rev. B* **92**, 054422 (2015).
72. Hayashi, T., Fujisawa, T., Cheong, H. D., Jeong, Y. H. & Hirayama, Y. Coherent manipulation of electronic states in a double quantum dot. *Phys. Rev. Lett.* **91**(22), 226804 (2003).
73. Petersson, K. D., Petta, J. R., Lu, H. & Gossard, A. C. Quantum coherence in a one-electron semiconductor charge qubit. *Phys. Rev. Lett.* **105**(24), 246804 (2010).
74. Shi, Z. *et al.* Coherent quantum oscillations and echo measurements of a Si charge qubit. *Phys. Rev. B* **88**(7), 075416 (2013).
75. Giavaras, G. & Tokura, Y. Spectroscopy of double quantum dot two-spin states by tuning the interdot barrier. *Phys. Rev. B* **99**(7), 075412 (2019).
76. Stehlik, J., Maialle, M. Z., Degani, M. H. & Petta, J. R. Role of multilevel Landau-Zener interference in extreme harmonic generation. *Phys. Rev. B* **94**, 075307 (2016).

Acknowledgements

This work was supported by the National Science Centre (NCN) according to decision DEC-2019/35/O/ST3/00097 and Polish National Agency for Academic Exchange (NAWA) under program Zagraniczne Staże Doktorskie NAWA Preludium BIS 1 according to decision PPN/STA/2021/1/00076/DEC/1. We gratefully acknowledge Poland's high-performance computing infrastructure PLGrid (HPC Center Cyfronet) for providing computer facilities and support within computational grant no. PLG/2024/017175. Research was partly supported by program "Excellence initiative - research university" for the AGH University of Krakow. We are sincerely grateful to Dr Diego Rabelo da Costa and Dr Andrey Chaves for very helpful discussions.

Author contributions

TT performed calculations, led the analysis of the results and wrote the manuscript. FMP and BS participated in setting the problem, selection of the calculation methods, analysis of the data and editing the manuscript.

Competing interests

The authors declare no competing interests.

Additional information

Correspondence and requests for materials should be addressed to B.S.